

## The hydrothermal synthesis of blue-emitting boron-doped CQDs and its application for improving the photovoltaic parameters of organic solar cell

Tuğbahan YILMAZ\* 

Department of Physics, Faculty of Science, Selcuk University, Konya, Turkey

Received: 05.04.2021 • Accepted/Published Online: 02.08.2021 • Final Version: 20.12.2021

**Abstract:** In this work, boron-doped CQDs (B-CQDs) were synthesized by using boric acid, urea, and citric acid via hydrothermal method to use as a novel additive material for poly(3-hexylthiophene-2,5-diyl) (P3HT):[6,6]-phenyl-C61-butyric acid methyl ester (PCBM) based organic solar cells. The OSCs with an inverted device structure were fabricated on titanium dioxide (TiO<sub>2</sub>) thin film. It was showed the crystallinity, morphological and optical properties of P3HT:PCBM films improved after B-CQDs additive. The best performance was obtained to be a 39.65% of FF, a 546 mV of V<sub>oc</sub>, an 8.606 mA cm<sup>-2</sup> of J<sub>sc</sub> after 3 vol.% B-CQDs addition in P3HT:PCBM blend. The power conversion efficiency (PCE) enhanced from 1.72% (non-doped device) to 2.33% (3% of B-CQDs) (a ~ 35% increase). The obtained results provided that B-CQDs are promising materials to improve the performance of solar cell applications. The novelty of this work is to improve the performance of OSCs using cost-effective and eco-friendly Boron CQDs as an additive. Besides, to achieve a good PCE of OSCs, it is necessary for utilized clean and green energy.

**Key words:** Additive material, boron doped CQDs, organic solar cell (OSC), P3HT: PCBM blend

### 1. Introduction

Organic solar cells (OSCs) have introduced some advantages such as large-area, low-cost, flexibility, light weight, easy fabrication *via* solution process; therefore, OSCs are highly attracted in renewable energy application [1,2]. The most investigated OSCs device structure is based on bulk heterojunction (BHJ), a continuous interpenetrating network of semiconductor materials, and fullerene derivative [2]. As a photoactive layer, poly (3-hexylthiophene-2,5-diyl) (P3HT) and (6, 6)-phenyl C61 butyric acid methyl ester (PCBM) are widely utilized in literature [3,4]. Over the last decade, researchers have reached a PCE of 18.69% with bulk heterojunction OSCs [5,6]. Although the solar cell efficiency has improved, further studies are needed to improve fill factor (FF) [7], short-circuit current density (J<sub>sc</sub>) [8] and open-circuit voltage (V<sub>oc</sub>) [9]. There are many approaches to enhance OSCs efficiency, including synthesis of low bandgap donor materials [10], optimization of device structure [11], improving the morphology of photoactive layer [12], using different fabrication techniques [13], interface modification [14], and incorporating additives in the active layer [15]. Within these approaches, the incorporation of additives is one of the versatile techniques to improve the power conversion efficiency of OSCs through the enhancement of morphology of photoactive layer at the nanoscale. Up to now, small molecules, metallic nanoparticles, solvents, and quantum dots have been studied as additives [16–20]. However, there is a lack of studies related to the incorporation of additives of QDs into active layer. On the other hand, most studies have centred on the using QDs based on cadmium sulphide (CdS), cadmium selenide (CdSe), cadmium telluride (CdTe), and lead sulphide (PbS) [21]. In addition, carbon based QDs have been studied to enhance the power conversion efficiency of OSCs [22,23].

Carbon quantum dots (CQDs) have caught attention with regard to its advantages such as a high carrier mobility, high conductivity, a wide absorption range, a narrow emission range, and stability [24]. Being able to control the size of CQDs can make possible the adjustment of the energy levels of the valence band and conduction band of CQDs, which can lead to use in different applications [25–27]. Furthermore, a number of techniques for the synthesis of CQDs have been demonstrated, including hydrothermal, microwave, laser ablation, arc discharge, acidic oxidation, electrochemistry, pyrolysis techniques [23,28–31]. CQDs are a great candidate for optoelectronic applications, including lighting emitting diodes (LEDs), field effect transistor (FETs), solar cells (SCs), and sensors due to these unique properties [23,32–35].

\* Correspondence: [tugbahanyilmazalic@selcuk.edu.tr](mailto:tugbahanyilmazalic@selcuk.edu.tr)

Recently, heteroatom doped CQDs such as boron (B), nitrogen (N), phosphor (P), and fluorine (F) have been synthesized and applied as an additive for optoelectronic devices [22,36]. The addition of CQDs is an effective pathway to control and improve the photoluminescence (PL) properties used to measure quantum yield [37]. Notwithstanding, there are limited studies with regard to doped CQDs, the studies so far have showed that the efficiency of photoluminescence increased after boron doped CQDs (B-CQDs) [38,39]. Additionally, similarly N doped CQDs, boron can cause to form good crystalline structure of CQDs, which is attributed to improving conductivity [40]. On the other hand, B-CQDs are good candidates for organic solar cell applications due to its excellent stability against storage, UV illumination time, temperature, and pH value [41]. In light of the previous studies, using B-CQDs could be one of pathway to enhance the photovoltaic performance of OSCs.

Herein, boron doped CQDs synthesis was achieved by hydrothermal method to use as an additive into the P3HT:PCBM blend. B-CQDs were introduced with various volumes into P3HT:PCBM blend to improve energy harvesting properties, crystal structure, and charge transport properties of photoactive layer. Thanks to improved morphology, better crystallinity, effective charge transfer, phase separation, and interchain interaction of photoactive layer could be obtained, which essentially ushers to increase PCE. The results showed that the morphological and optical properties of P3HT:PCBM films and its crystallinity improved after the addition of B-CQDs. Compared to non-doped films, PCE increased from 1.72% (non-doped device) to 2.33% (%3 of B-CQDs additive). Additionally, a good crystalline structure of P3HT:PCBM layer was obtained after addition of B-CQDs of a good, which leads to increase PCE. After 3 vol.% of B-CQDs additive, the best photovoltaic parameter was achieved the PCE 2.33% with a 39.65% of FF, a 546 mV of  $V_{oc}$ , an 8.606 mA  $cm^{-2}$  of  $J_{sc}$ . The results clearly indicated that doping B-CQDs into P3HT:PCBM blend improved the solar cell performance.

## 2. Experimental

### 2.1. Synthesis of B-CQDs

B-CQDs synthesis procedure is shown in Figure 1. In a typical procedure, boric acid (4 g) (Merck), urea (4 g) (Sigma-Aldrich, 99%), and citric acid (4 g) (Sigma-Aldrich, 99%) were dissolved in deionized (DI) water (80 mL) [42]. Boric acid was used as boron source, while urea and citric acid were used as carbon source.

The prepared solution was mixed and transferred into stainless-steel autoclave for hydrothermal synthesis of B-CQDs at 120 °C for 12 h and then cooled to room temperature. Afterwards, the obtained solution was centrifugated at 6000 rpm for 10 min. After the excess water had been removed, remaining solid particles were dried in the oven at 80 °C for 24 h. B-CQDs solution was prepared by dispersing of certain amount of B-CQDs (10 mg/mL) in chlorobenzene.

### 2.2. Device fabrication

The structure of OSCs and corresponding energy level diagram are shown in Figure 2(a)&(b). Fluorine-doped tin oxide coated substrates (1.5 cm × 1.5 cm) were cleaned by diluted Hellmanex detergent solution (Sigma Aldrich, Hellmanex III), deionized water (DI), acetone, and isopropanol in an ultrasonic cleaner for 10 min, respectively. To remove organic traces, cleaned FTO surfaces were subjected to oxygen plasma treatment using a plasma cleaner (Diener Plasma System Femto PCCE-Plasma Cleaner) for 5 min after dried with  $N_2$ . To form a compact- $TiO_2$  (c- $TiO_2$ ) layer, cleaned FTO surfaces were spin-coated by solution mixture of titanium (IV) isopropoxide (99.9%, Sigma-Aldrich) and acetyl acetone (99.5%, Sigma-

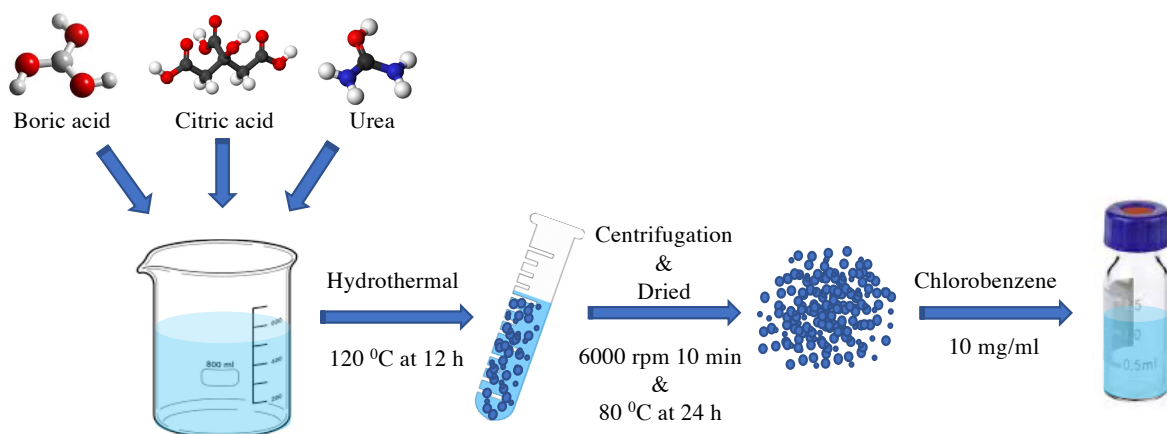
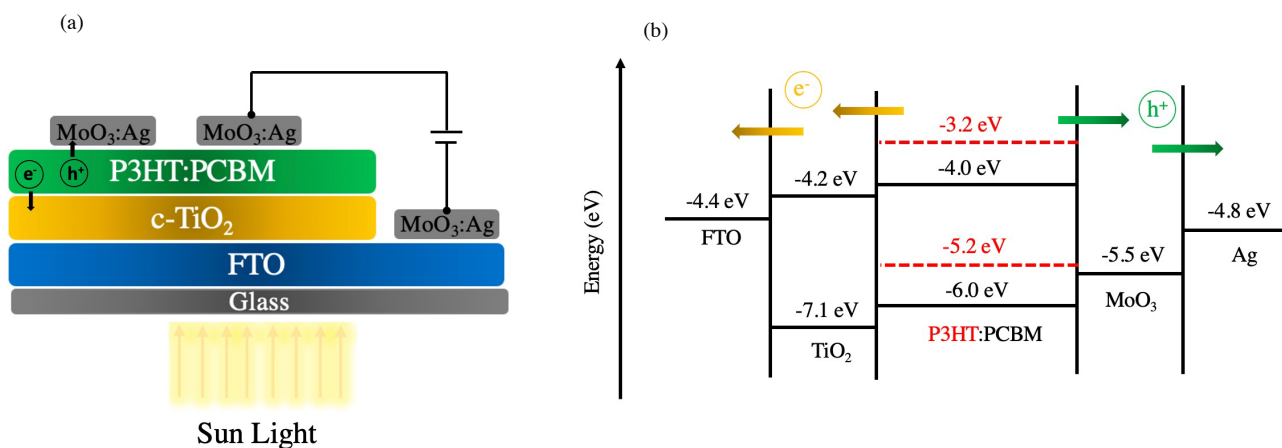


Figure 1. Synthesis process of B-CQDs.



**Figure 2.** The energy conversion mechanism and energy levels of fabricated OSCs.

Aldrich) with absolute ethanol as a precursor solution with a spinning speed of 3000 rpm for 20 s, following 2500 rpm for 20 s, and then all  $\text{TiO}_2$  coated substrates were left on hot plate at  $110\text{ }^\circ\text{C}$  for 10 min. Afterwards, sintering of FTO with  $\text{TiO}_2$  substrates was completed at  $450\text{ }^\circ\text{C}$  for 1 h in air. Then, all substrates were cooled down at room temperature before the active layer deposition.

To obtain an active layer, P3HT (Sigma-Aldrich):PCBM (Lumtec) blend solution was dissolved a 40 mg/mL in chloroform (CF): chlorobenzene (CB) (1:1) at 1.0:0.6 weight ratio, and then the prepared P3HT:PCBM solution was stirred at  $70\text{ }^\circ\text{C}$  overnight. The B-CQDs particles were dissolved in chlorobenzene at a 10 mg/mL to prepare dopant solution. Subsequently, prepared-P3HT:PCBM solution was doped with three various concentrations of B-CQDs solution (1 vol.%, 3 vol.% and 5 vol.%) after P3HT:PCBM solution filtered by polytetrafluoroethylene (PTFE) filter with  $0.22\text{ }\mu\text{m}$ . The P3HT:PCBM solution with non-doped and doped was deposited on the  $\text{c-TiO}_2$  layer by spin-coating at 2200 rpm for 30 s, followed by 2500 rpm for 30 s. Then all coated substrates were heated at  $160\text{ }^\circ\text{C}$  for 10 min. To finalize the device fabrication, 10 nm thickness  $\text{MoO}_3$  and 80 nm thickness Ag electrodes were deposited by thermal under about  $10^{-6}$  mbar vacuum pressure through a shadow mask ( $0.023\text{ cm}^2$  active area).

### 2.3. Characterization

The photoluminescent (PL) spectra of B-CQDs solution was taken by photoluminescent spectrometer (Perkin Elmer LS-55) with 350 nm excitation wavelength. The structure of B-CQDs was analysed by Transmission Electron Microscope (TEM, JEOL, Akishimashi, Tokyo, Japan) operated at 200 kV. The optical properties of B-CQDs solution and non-doped and doped B-CQDs P3HT:PCBM films were analysed by an ultraviolet-visible (UV-Vis) absorption spectrometer (Biochrom Libra S22) from 250 nm to 550 and 300 nm to 800 nm, respectively. The thickness of thin films was measured using a profilometer (NanoMap-LS). The morphology of non-doped and doped with B-CQDs P3HT:PCBM films was examined using an Atomic Force Microscope (AFM, NT-MDT NTEGRA Solaris). AFM images were taken in "tapping mode". To understand the influence of the addition of B-CQDs on P3HT:PCBM film crystallization, all P3HT:PCBM layer with non-doped and doped B-CQDs were analysed by X-ray diffraction spectrometer (XRD, Bruker Advance D8) with  $\text{Cu K}\alpha$  radiation at a wavelength of  $1.5406\text{ \AA}$  at 40 kV. The presence of boron element was measured The Scanning Electron Microscopy with Energy Dispersive X-Ray (SEM-EDX, Zeiss EVO LS 10) analysis. The current density-voltage ( $J-V$ ) curves of the fabricated OPVs were determined by ATLAS solar simulator using a Keithley 2400 Source under illumination of a simulated sunlight ( $\text{AM } 1.5, 80\text{ mW cm}^{-2}$ ) in the glovebox.

## 3. Results and discussion

### 3.1. Structural, optical and morphological characterization of B-CQDs

It is clear from Figure 3(a), B-CQDs shows a uniform distribution. TEM image indicated that B-CQDs are mostly of spherical form and well-dispersed as shown in Figure 3(b). In addition, B-CQDs were measured with a mean diameter of nearly 10 nm. Particle sizes are seen to be between less than 6 nm after zoomed into TEM image, which matches with our previous study [43].

For further details in the optical and structural properties of B-CQDs, UV-Vis absorption spectra (black line) and PL spectra (red line) were taken as shown Figure 4. The UV-Vis absorption spectra (black line) indicated that the peaks

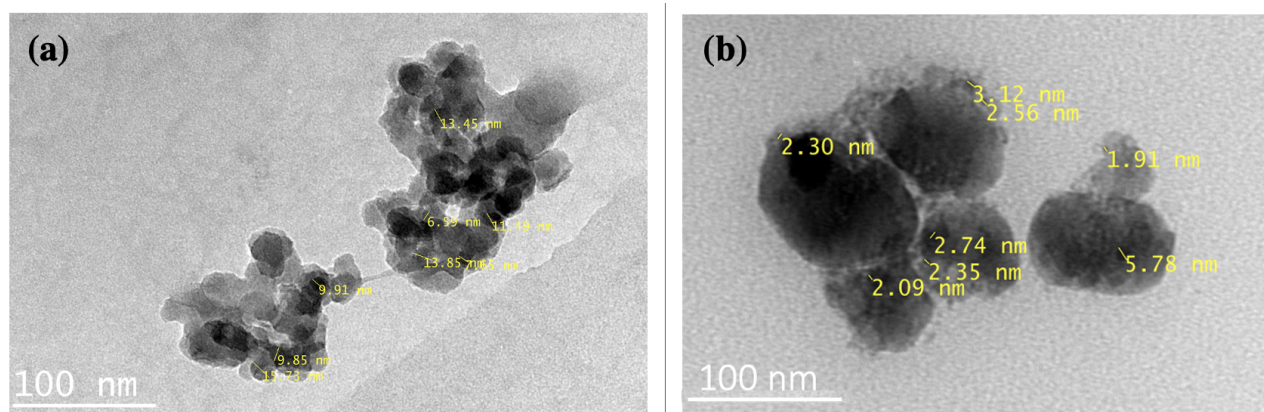


**Figure 3.** The TEM images of B-CQDs.

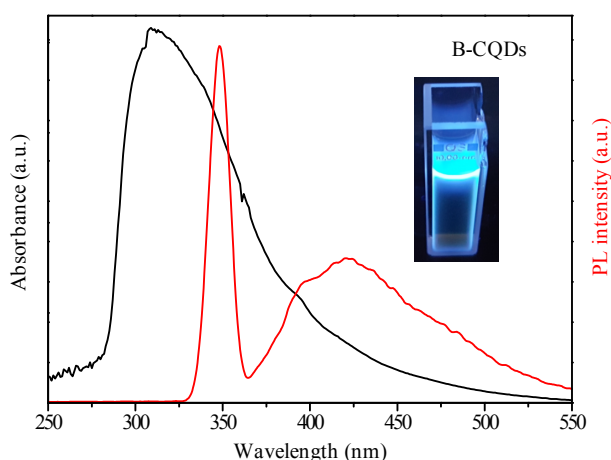


**Figure 4.** The measured UV-Vis absorption spectra (black) and photoluminescence (PL) spectra (red) of B-CQDs under the excitation wavelength of 350 nm [Inset: Photographs of B-CQDs under UV-light].

observed at around 330 nm. The  $\lambda_{\max}$  is attributed to  $n-\pi^*$  transition of carbonyl bonds [30,44]. In addition, according to PL spectrum (red line), a slightly strong emission was observed at around 425 nm while excitation at 350 nm as well as correspond to bright blue light under UV light was shown in the inset of Figure 4. Further, the results clearly showed that B-CQDs has a high fluorescent property in the blue spectral region, which is associated with the optical properties of the quantum dots [31,45, 46].

To measure quantum yield (QY) of B-CQDs, coumarin 2 solution was dissolved at  $10^{-7}$  M in ethanol as a reference ( $QY_0=0.68$ ) [47] and the QY of B-CQDs in deionized water at different concentration. Horiba Scientific's guide to measurement of fluorescence QY is used for QY calculation [48]. Afterwards, QY of B-CQDs is calculated by following equation (1),

$$QY_{B-CQDs} = QY_0 \left( \frac{m}{m_0} \right) \left( \frac{\eta^2}{\eta_0^2} \right) \quad (1)$$

where  $QY_{B-CQDs}$  and  $QY_0$  are QY of B-CQDs and Coumarin, respectively.  $m$  is the slope value, and  $\eta$  is the refractive index of solvent. Here,  $\eta$  and  $\eta_0$  values are 1.333 and 1.36, respectively. Figure 5 depicts the fluorescence responses of the B-CQD with different concentrations. Furthermore, the relationship between  $F/F_0$  and the concentration is shown in the Figure 5 inset. The QY of B-CQDs is calculated to be 12.41% by using Coumarin 2 as a reference. This result is integrated with previous studies in literature [38,39]. The quantum yields show that the B-CQDs as an electron acceptor can act as a

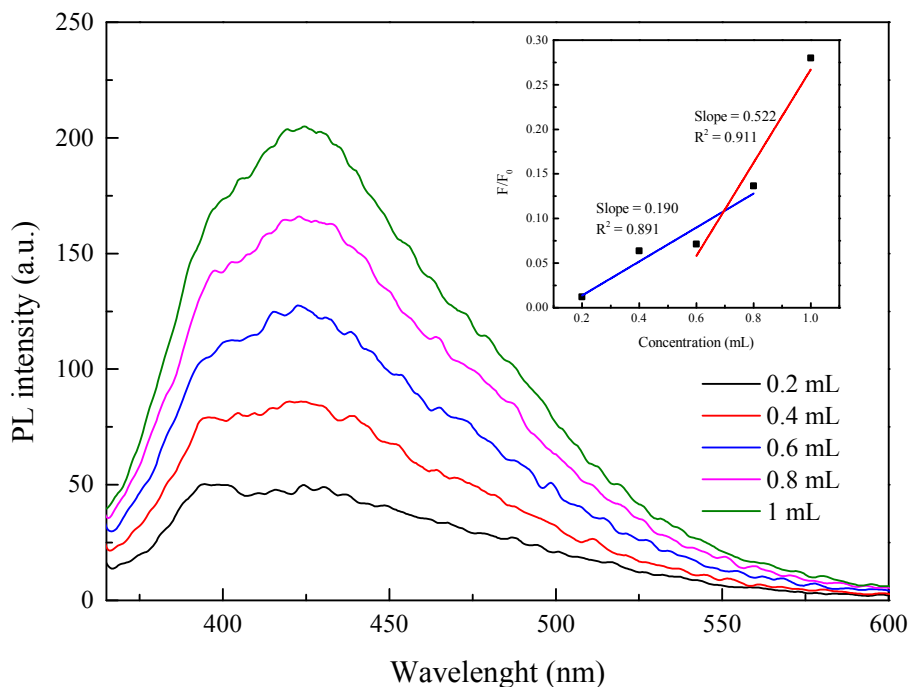


**Figure 5.** The fluorescence responses of the B-CQD with different concentrations (inset: the relationship between  $F/F_0$  and the concentrations).

driving force for charge transfer, especially in the excited state [39]. Therefore, it could lead to improve the performance parameters of OSCs.

### 3.2. Optical and morphological characterization of organic photoactive layer

To understand the addition of B-CQDs into P3HT:PCBM blend, optical absorption spectra and optical band gaps ( $E_g$ ) of non-doped and B-CQDs doped films were studied by UV-Vis spectrometer in the range of 300–800 nm. As seen in Figure 6, the optical absorption of P3HT:PCBM films showed similar characteristics and was observed around at 500 nm, which is correlated with previous studies [49,50]. Additionally, the first absorption shoulder was exhibited around at 330 nm referred to PCBM and a dominant peak at 500 nm attributed to P3HT. The dominant peak could be related to one exciton and two photons' generations [51]. The results also showed that the intensity of absorption peaks increased after addition of B-CQDs into blend.

The optical band gaps' ( $E_g$ ) values of P3HT:PCBM films were determined from the intercept of  $(\alpha hv)^2$  vs.  $(hv)$  curves [52], as shown in Figure 7, by the following equation (2):

$$(\alpha hv)^2 = A (hv - E_g) \quad (2)$$

where  $\alpha$ ,  $hv$ , and  $A$  are the absorption coefficient, photon energy, independent constant, respectively. The average thickness of P3HT:PCBM films was about 200 nm. The  $E_g$  values were increased from 3.785 eV for non-doped P3HT:PCBM film to 3.816 eV and 3.807 eV for 3 vol.% of B-CQDs and 5 vol.% of B-CQDs, respectively, while it decreased to 3.778 eV for 1 vol.% of B-CQDs, as seen in Table 1.

As known, the  $E_g$  values of P3HT:PCBM film depend on the concentration of P3HT:PCBM film as well as thickness of P3HT:PCBM film [53,54]. Besides, the electrical parameters of OSC are affected by increased  $E_g$  values due to the chemical composition of P3HT, good crystallinity, and as a result of the gap states formation. Therefore, it can be stated that there is a correlation between the optical properties and the electrical parameters of OSC [55].

The crystallinity of active layer is important for improving device performance since it does not hinder the charge transport [56]. Therefore, to investigate the crystallinity of non-doped and B-CQDs doped P3HT:PCBM films, the XRD pattern was recorded in the range of  $5^\circ$ – $70^\circ$ . The XRD spectra are presented in Figure 8. As seen in Figure 8(a), the P3HT (100) diffraction peak was observed around a  $2\theta$  value of  $5.4^\circ$ , while no significant difference corresponding d-space of 1.161 nm between the XRD patterns of non-doped and B-CQDs doped P3HT:PCBM films. It appears that the intensity of the XRD peaks clearly increased after adding 3 vol.% and 5 vol.% B-CQDs, while the intensity of XRD peak slightly decreased after adding 1 vol.% B-CQDs, indicating an improvement in crystallite size for addition of 3 vol.% of B-CQDs

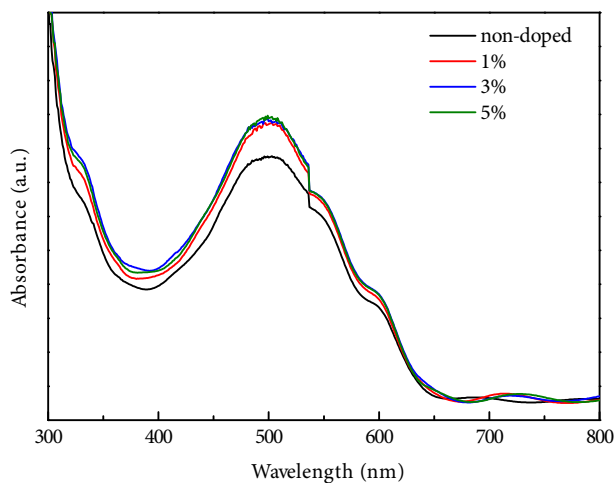


**Figure 6.** The measured UV-Vis absorption spectra of the non-doped and doped films of P3HT:PCBM.

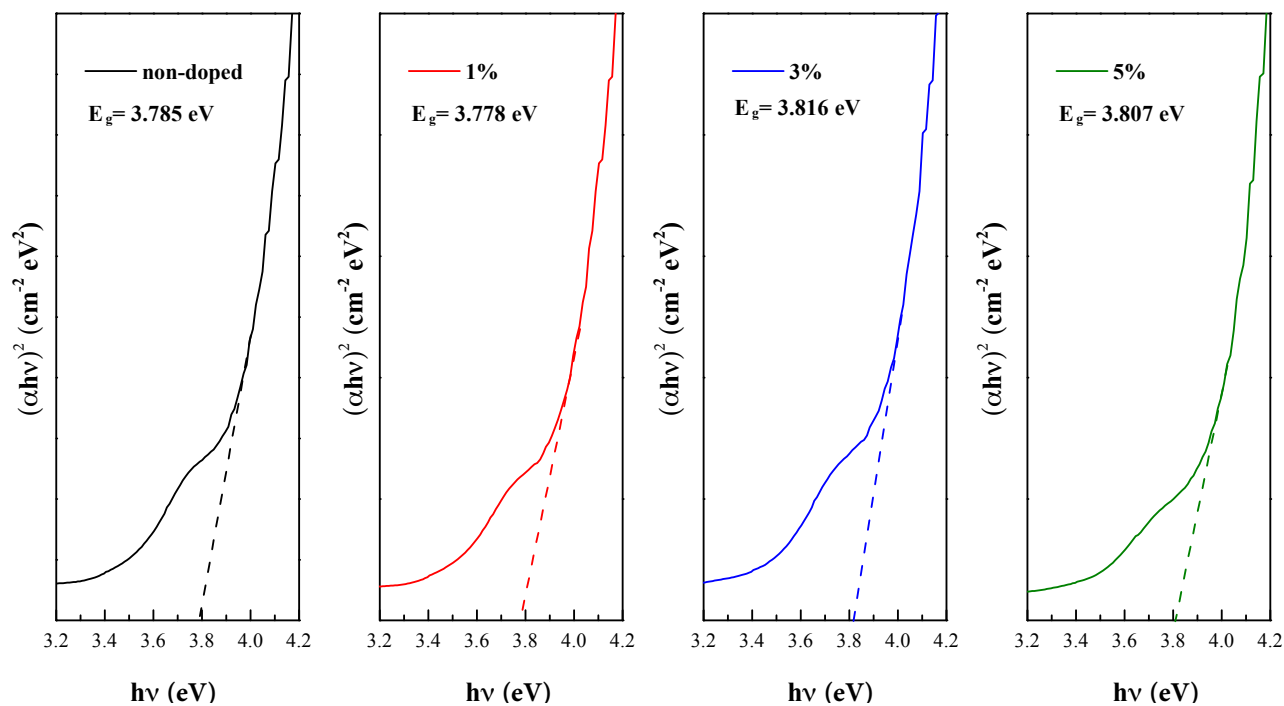


**Figure 7.** The measured optical band gap extracted from Tauc's plot of the non-doped and doped films of P3HT:PCBM.

**Table 1.** The optical band gap, crystal size, and roughness values of non-doped and doped B-CQDs P3HT:PCBM films.

	$E_g$ (eV)	Crystallite size (nm)	Roughness (nm)
Non-doped	3.785	38.61	3.508
1 vol.% of B-QCDs	3.778	37.68	2.280
3 vol.% of B-QCDs	3.816	39.99	2.344
5 vol.% of B-QCDs	3.807	39.79	2.788

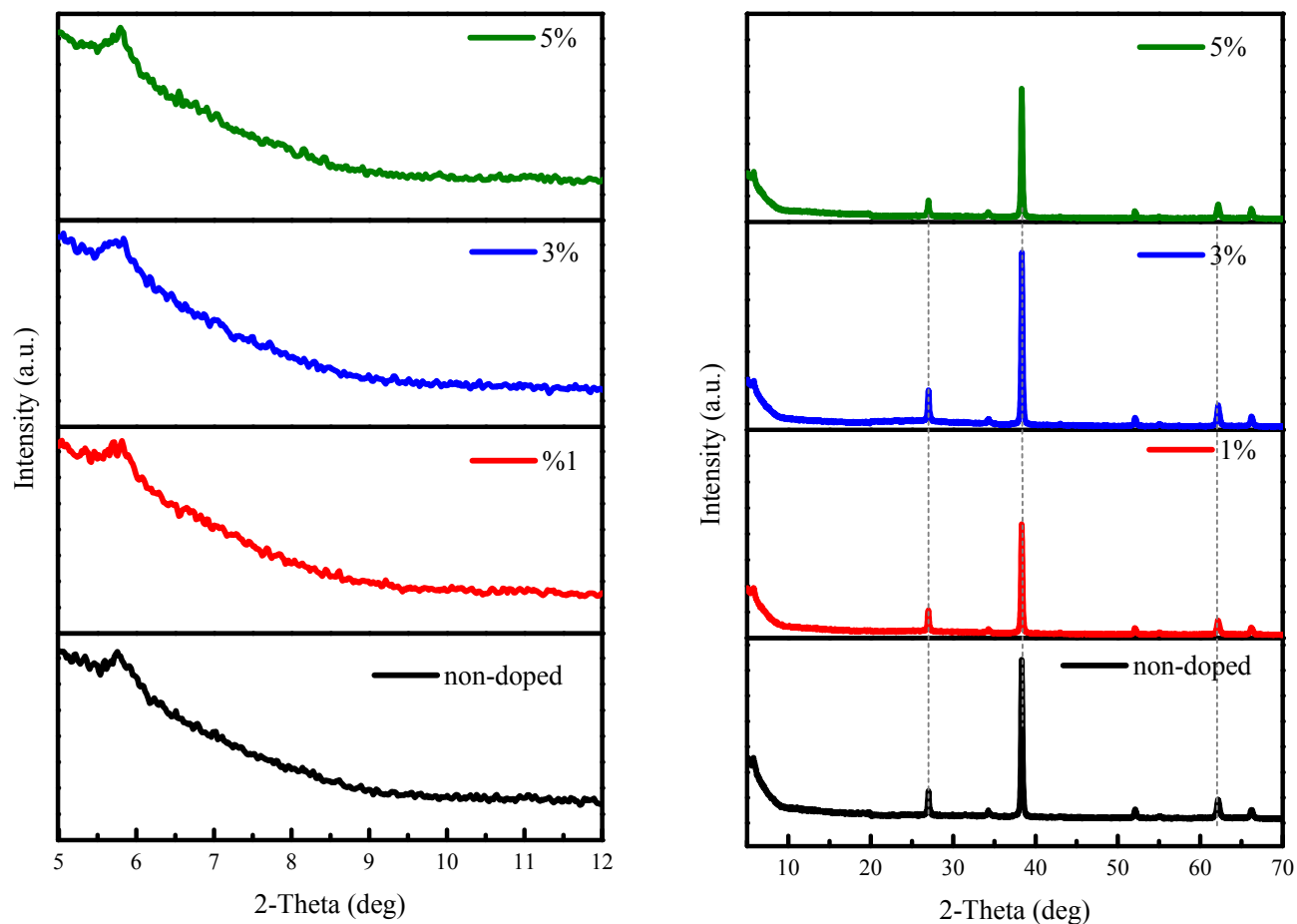


**Figure 8.** The X-ray diffraction (XRD) spectra of the non-doped and doped films of P3HT:PCBM.

and 5 vol.% of B-CQDs, as shown in Figure 8(b). The mean sizes of these films' crystallite were extracted from Scherrer equation, which are also summarized in Table 1 [57]. The results showed that the crystallite sizes of P3HT:PCBM films increased from 38.61 nm for non-doped to 39.99 nm for 3 vol.% and 39.79 nm for 5 vol.% of B-CQDs, respectively, whereas decreased to 37.68 nm for 1 vol.% of B-CQDs. Based on these results, it can be said that CQDs are good candidates for obtaining good crystallites [58]. These results provide that the charge transport properties of P3HT:PCBM films could be improved after the addition of B-CQDs, thus the performance parameters of OSCs tend to improve.

In Figure 9, the presence of boron element in CQDs was performed by SEM-EDX mapping analysis. As shown in Figure 9(b), besides the XRD analysis, EDS mapping were performed for further investigation of the B-CQDs composition. The SEM-EDX results showed that they consist of three elements: oxygen, carbon, and boron at the amount of 57.22%, 33.70% and 9.08%, respectively, as given in Figure 9(c). Oxygen can be associated with the functional groups on the CQDs, while the main element of CQD is carbon. As a result, the presence of boron in the CQDs was clearly observed by EDX analysis.

The microstructure of organic photoactive layer plays a significant role in the electrical parameters of OSC, thereby, the surface morphology of non-doped and B-CQDs doped P3HT:PCBM films was studied by atomic force microscope (AFM) technique, and all AFM image processing were performed by WSxM 5.0 software [59]. AFM images are presented in Figure 10, and the average roughness ( $R_a$ ) values are also summarized in Table 1. As seen, the  $R_a$  of non-doped and B-CQDs doped P3HT:PCBM film were measured to be 3.508 nm for non-doped film, 2.280 nm for doping 1 vol.% of B-CQDs, 2.344 nm for doping 3 vol.% of B-CQDs, and 2.788 nm for doping 5 vol.% of B-CQDs. The results indicate that a lower surface roughness was obtained after adding B-CQDs. To improve electrical parameter of OSC, the optimization of B-CQDs concentration has a great influence on the charge transport properties of organic photoactive layer due to its surface morphology.

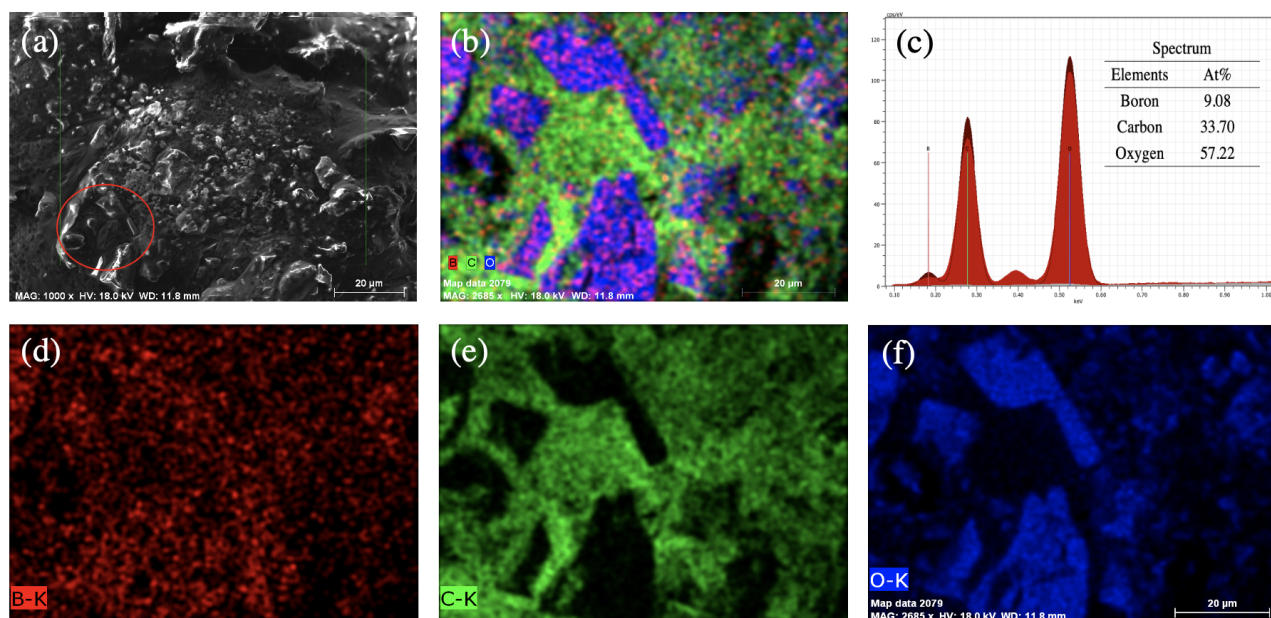


**Figure 9.** SEM-EDX mapping analysis of B-CQDs. (a) EDX mapping based SEM image of B-CQDs. (b) The elemental mapping of B-CQDs showing, (c) EDX representation of the B-CQDs, the inset image shows the elemental composition percentage in B-CQDs. (d) B-K series, (e) C-K series, and (f) O-K series.

### 3.4. Device characterization

The structure of final device had a configuration with FTO / TiO<sub>2</sub> (90 nm) / P3HT:PCBM (200 nm) / MoO<sub>3</sub> (10 nm):Ag (80 nm). To figure out the effect of B-CQDs content on the electrical parameters of OSCs, the devices were fabricated with non-doped and doped of BCQDs into the photoactive layer. The photovoltaic performance of as-prepared devices was measured under light and dark conditions, as shown in Figures 11(a)&(b), and the photovoltaic parameters are also summarized in Table 2.

The non-doped OSC presents a fill factor (FF) of 31.77%, a short circuit current density ( $J_{sc}$ ) of 8.437 mA cm<sup>-2</sup>, open-circuit voltage ( $V_{oc}$ ) of 515 mV, and a lower PCE value of 1.72%. Compared to non-doped OSC, the best photovoltaic performance of OSC doping 3 vol.% B-CQDs was depicted a PCE of 2.33%, which was calculated from FF of 39.65%,  $V_{oc}$  of 546 mV, and  $J_{sc}$  of 8.606 mA cm<sup>-2</sup>. The increase in short circuit current density ( $J_{sc}$ ) and fill factor (FF) are the main reasons for the improvement of PCE [60]. As known, addition of CQDs is also affected on these parameters in terms of carrier mobility, trap density, carrier lifetime, and diffusion length [61]. Therefore, the effect of doping B-CQDs with various concentration on FF increased from 31.77% to 33.30%, 39.65%, and 36.04% for 1 vol.%, 3 vol.%, and 5 vol.% of B-CQDs doped, respectively. The values of  $J_{sc}$  increased from 8.337 mA cm<sup>-2</sup> to 8.606 mA cm<sup>-2</sup> and 9.264 mA cm<sup>-2</sup> for doping 3 vol.% and 5 vol.% of B-CQDs P3HT:PCBM, respectively, while decreased to 8.034 mA cm<sup>-2</sup> for doping 1 vol.% of B-CQDs. Although there is no big difference between non-doped and 1 vol.% of B-CQDs in terms of FF and  $J_{sc}$ , a low PCE of 1.62% was observed for 1 vol.% of B-CQDs doped, which is related to a low  $V_{oc}$  of 484 mV. Furthermore, the photovoltaic performance of 1 vol.% of B-CQDs doped OSCs may obtain a lowest PCE because of the factors such as crystallinity of active layer, morphology, and the trap density that can effect  $V_{oc}$  [62,63]. These results are also related to the morphological and structural properties of non-doped and B-CQDs doped P3HT:PCBM films.

As is known, the  $R_s$  plays an important role for determining the FF and the  $J_{sc}$ . Increasing FF could be associated with obtaining better device performance after the additive of B-CQDs to improve photovoltaic performance. This could be attributed to reduce serial resistance ( $R_s$ ) while increase shunt resistance ( $R_{sh}$ ) values [64]. The values of  $R_s$  and  $R_{sh}$  were measured from J-V curves obtained under illuminated condition, which are summarized in Table 2. The  $R_s$  values with B-CQDs additive showed a dramatical decrease from 30.79 Ω cm<sup>-2</sup> (non-doped) to 20.53 Ω cm<sup>-2</sup>, to 12.65 Ω cm<sup>-2</sup> and to 14.46 Ω cm<sup>-2</sup> with 1 vol.%, 3 vol.%, and 5 vol.% of B-CQDs additive, respectively. Moreover, the  $R_{sh}$  values with B-CQDs additive were increased from 97.65 Ω cm<sup>-2</sup> to 147.62 Ω cm<sup>-2</sup>, to 210.88 Ω cm<sup>-2</sup> and to 176.55 Ω cm<sup>-2</sup> with 1 vol.%, 3 vol.%, and 5 vol.% of B-CQDs additive, respectively. The  $R_{sh}$  is attributed to leakage current and charge transport properties. Therefore, the lowest 12.65 Ω cm<sup>-2</sup> of  $R_s$  and the highest 210.88 Ω cm<sup>-2</sup> of  $R_{sh}$  were obtained from OSCs with 3

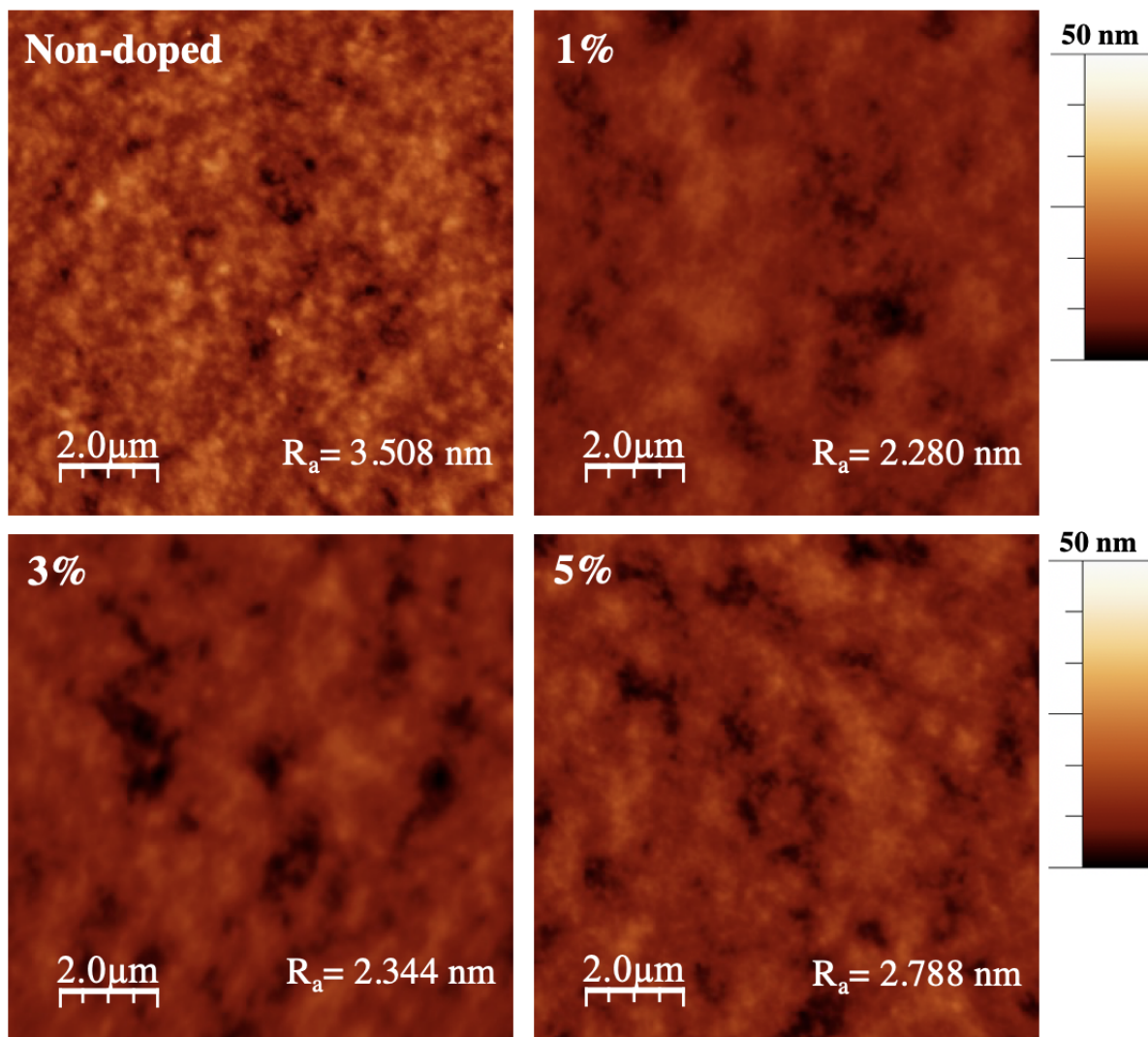


Figure 10. AFM images of the non-doped and doped films of P3HT:PCBM.

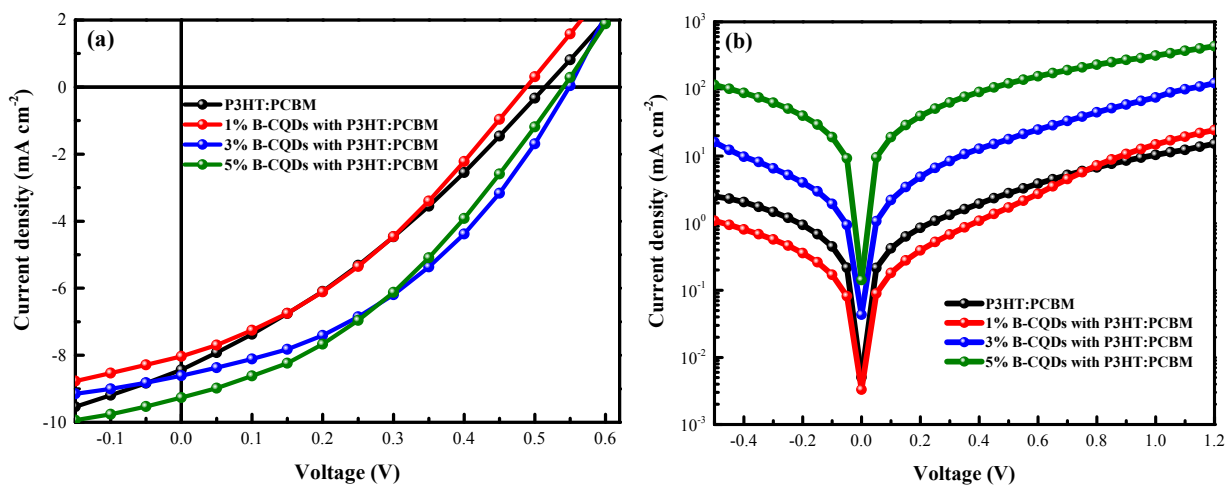


Figure 11. Current density-voltage ( $J$ - $V$ ) curves of all the OSCs with various volume of B-CQDs (a) under illumination of AM 1.5 G,  $80 \text{ mW cm}^{-2}$ , (b) in the dark.

**Table 2.** Device figure-of-merit parameters of the organic solar cells. Non-doped and doped B-CQDs under illumination of AM 1.5, 80 mW/cm<sup>2</sup>.

	FF (%)	V <sub>oc</sub> (mA)	J <sub>sc</sub> (mA cm <sup>-2</sup> )	PCE (%)	R <sub>s</sub> (Ω cm <sup>-2</sup> )	R <sub>sh</sub> (Ω cm <sup>-2</sup> )
Non-doped	31.77	0.515	8.437	1.72	30.79	97.65
1 vol.% of B-CQDs	33.30	0.484	8.034	1.62	20.53	147.62
3 vol.% of B-CQDs	39.65	0.546	8.606	2.33	12.65	210.88
5 vol.% of B-CQDs	36.04	0.538	9.264	2.25	14.46	176.55

vol.% of B-CQDs additive into P3HT:PCBM blend. The results show that the charge transport properties are improved by integrating perfectly with increasing FF values [43].

#### 4. Conclusion

In this study, boron doped CQDs were synthesized for use as additive in P3HT:PCBM blend as an photoactive layer to improve photovoltaic parameters. The device with the 3 vol.% B-CQDs additive P3HT:PCBM device showed 39.65% of FF, 546 mV of V<sub>oc</sub>, 8.606 mA cm<sup>-2</sup> of J<sub>sc</sub>, which led to a 2.33% of PCE (a 35% increasing). In addition, the lowest 12.65 Ω cm<sup>-2</sup> of R<sub>s</sub> and the highest 210.88 Ω cm<sup>-2</sup> of R<sub>sh</sub> are calculated with 3 vol.% of B-CQDs addition. After the addition of B-CQDs in the photoactive solution, charge transport properties were enhanced. The FF and the J<sub>sc</sub> values were increased by virtue of an improvement P3HT crystallinity as well as morphological and structural properties. The obtained results indicate that the heteroatom doped CQDs is an excellent candidate to the improvement of highly efficient OSCs.

#### Conflict of interest

The authors declare that they have no known competing financial interests or personal relationships that could have appeared to influence the work reported in this paper.

#### Acknowledgments

The author would like to thank to Dr. Çisem Kırbıyık Kurukavak for her helpful advice and comments.

#### References

- Chen LX. Organic Solar Cells: Recent Progress and Challenges. ACS Energy Letters 2019; 4: 2537-2539. doi: 10.1021/acscenergylett.9b02071
- Wang G, Melkonyan FS, Facchetti A, Marks TJ. All-Polymer Solar Cells: Recent Progress, Challenges, and Prospects. Angewandte Chemie International Edition 2019; 58: 4129-4142. doi: 10.1002/anie.201808976
- Abdallaoui M, Sengouga N, Chala A, Meftah AF, Meftah AM. Comparative study of conventional and inverted P3HT: PCBM organic solar cell. Optical Materials 2020; 105: 109916. doi: 10.1016/j.optmat.2020.109916
- Chen D, Zhang C, Wang Z, Zhang J, Feng Q et al. Performance Comparison of Conventional and Inverted Organic Bulk Heterojunction Solar Cells From Optical and Electrical Aspects. IEEE Transactions on Electron Devices 2013; 60: 451-457. doi: 10.1109/TED.2012.2224114
- Jin K, Xiao Z, Ding L. D18, an eximious solar polymer!. Journal of Semiconductors 2021; 42(1): 010502, doi: 10.1088/1674-4926/42/1/010502
- Jin K, Xiao Z, Ding L. 18.69% PCE from organic solar cells. Journal of Semiconductors 2021; 42 (6): 060502. doi: 10.1088/42/6/060502
- Jao MH, Liao HC, Su WF. Achieving a high fill factor for organic solar cells. Journal of Materials Chemistry A 2016; 4: 5784-5801. doi: 10.1039/C6TA00126B
- Lee TH, Choi MH, Jeon SJ, Nam SJ, Han YW et al. Improvement of short circuit current density by intermolecular interaction between polymer backbones for polymer solar cells. Polymer Journal 2017; 49: 177-187. doi: 10.1038/pj.2016.104
- Nolasco JC, Castro-Carranza A, Leon YA, Briones-Jurado C, Gutowski J et al. Understanding the open circuit voltage in organic solar cells on the basis of a donor-acceptor abrupt (p-n++) heterojunction. Solar Energy 2019; 184: 610-619. doi: 10.1016/j.solener.2019.04.031
- Li X, Guo J, Yang L, Chao M, Zheng L et al. Low Bandgap Donor-Acceptor π-Conjugated Polymers From Diarylcyclopentadienone-Fused Naphthalimides. Frontiers in Chemistry 2019; 7. doi: 10.3389/fchem.2019.00362

11. Zhang S, Ye L, Zhao W, Yang B, Wang Q, Hou J. Realizing over 10% efficiency in polymer solar cell by device optimization. *Science China Chemistry* 2015; 58: 248-256. doi: 10.1007/s11426-014-5273-x
12. Cui C, Li Y. Morphology optimization of photoactive layers in organic solar cells. *Aggregate* 2021; 2 (2): 1-13. doi: 10.1002/agt2.31
13. Peet J, Senatore ML, Heeger AJ, Bazan GC. The Role of Processing in the Fabrication and Optimization of Plastic Solar Cells. *Advanced Materials* 2009; 21: 1521-1527. doi: 10.1002/adma.200802559
14. Kırbıyık Kurukavak Ç, Yılmaz T, Büyükbekar A, Kuş M. Effect of different terminal groups of phenyl boronic acid self-assembled monolayers on the photovoltaic performance of organic solar cells. *Optical Materials* 2021; 112: 110783. doi: 10.1016/j.optmat.2020.110783
15. Sai-Anand G, Dubey A, Gopalan AI, Venkatesan S, Ruban S et al. Additive assisted morphological optimization of photoactive layer in polymer solar cells. *Solar Energy Materials and Solar Cells* 2018; 182: 246-254. doi: 10.1016/j.solmat.2018.03.031
16. Wu W, Wu H, Zhong M, Guo S. Dual Role of Graphene Quantum Dots in Active Layer of Inverted Bulk Heterojunction Organic Photovoltaic Devices. *ACS Omega* 2019; 4: 16159-16165. doi: 10.1021/acsomega.9b02348
17. Gao H, Meng J, Sun J, Deng J. Enhanced performance of polymer solar cells based on P3HT:PCBM via incorporating Au nanoparticles prepared by the micellar method. *Journal of Materials Science: Materials in Electronics* 2020; 31: 10760-10767. doi: 10.1007/s10854-020-03626-x
18. Song X, Gasparini N, Baran D. The Influence of Solvent Additive on Polymer Solar Cells Employing Fullerene and Non-Fullerene Acceptors. *Advanced Electronic Materials* 2017; 4. doi: 10.1002/aelm.201700358
19. Gollu SR, Sharma R, Srinivas G, Kundu S, Gupta D. Incorporation of silver and gold nanostructures for performance improvement in P3HT: PCBM inverted solar cell with rGO/ZnO nanocomposite as an electron transport layer. *Organic Electronics* 2016; 29: 79-87. doi: 10.1016/j.orgel.2015.11.015
20. Xu B, Sai-Anand G, Gopalan, AI, Qiao Q, Kang SW. Improving Photovoltaic Properties of P3HT:IC(60)BA through the Incorporation of Small Molecules. *Polymers (Basel)* 2018; 10: 121. doi: 10.3390/polym10020121
21. Manivannan R, Victoria SN. Preparation of chalcogenide thin films using electrodeposition method for solar cell applications – A review. *Solar Energy* 2018; 173: 1144-1157. doi: 10.1016/j.solener.2018.08.057
22. Kandasamy G. Recent Advancements in Doped/Co-Doped Carbon Quantum Dots for Multi-Potential Applications. *Journal of Carbon Research* 2019; 5 (2): 24. doi: 10.3390/c5020024
23. Cao L, Shiral Fernando KA, Liang W, Seilkop A, Monica Veca L et al. Carbon dots for energy conversion applications. *Journal of Applied Physics* 2019; 125: 220903. doi: 10.1063/1.5094032
24. Li Z, Zhao S, Xu Z, Wageh S, Song D et al. Improving charge transport by the ultrathin QDs interlayer in polymer solar cells. *RSC Advances* 2018; 8: 17914-17920. doi: 10.1039/C8RA02770F
25. Tetsuka H, Nagoya A, Fukusumi T, Matsui T. Molecularly Designed, Nitrogen-Functionalized Graphene Quantum Dots for Optoelectronic Devices. *Advanced Materials* 2016; 28: 4632-4638. doi: 10.1002/adma.201600058
26. Ryu J, Lee JW, Yu H, Yun J, Lee K et al. Size effects of a graphene quantum dot modified-blocking TiO<sub>2</sub> layer for efficient planar perovskite solar cells. *Journal of Materials Chemistry A* 2017; 5 (32): 16834-16842. doi: 10.1039/C7TA02242E
27. Sadhanala HK, Nanda KK. Boron-doped carbon nanoparticles: Size-independent color tunability from red to blue and bioimaging applications. *Carbon* 2016; 96: 166-173. doi: 10.1016/j.carbon.2015.08.096
28. Dey S, Govindaraj A, Biswas K, Rao CNR. Luminescence properties of boron and nitrogen doped graphene quantum dots prepared from arc-discharge-generated doped graphene samples. *Chemical Physics Letters* 2014; 595-596: 203-208. doi: 10.1016/j.cplett.2014.02.012
29. Ge S, He J, Ma C, Liu J, Xi F, Dong X. One-step synthesis of boron-doped graphene quantum dots for fluorescent sensors and biosensor. *Talanta* 2019; 199: 581-589. doi: 10.1016/j.talanta.2019.02.098
30. Fan Z, Li Y, Li X, Fan L, Zhou S et al. Surrounding media sensitive photoluminescence of boron-doped graphene quantum dots for highly fluorescent dyed crystals, chemical sensing and bioimaging. *Carbon* 2014; 70: 149-156. doi: 10.1016/j.carbon.2013.12.085
31. Pal A, Ahmad K, Dutta D, Chattopadhyay A. Boron Doped Carbon Dots with Unusually High Photoluminescence Quantum Yield for Ratiometric Intracellular pH Sensing. *ChemPhysChem* 2019; 20: 1018-1027. doi: 10.1002/cphc.201900140
32. Yuan F, Yuan T, Sui L, Wang Z, Xi Z et al. Engineering triangular carbon quantum dots with unprecedented narrow bandwidth emission for multicolored LEDs. *Nature Communications* 2018; 9: 2249. doi: 10.1038/s41467-018-04635-5
33. Mohanraj J, Durgalakshmi D, Prabha S, Saravanan R, Vo DVN et al. Green synthesis of white light emitting carbon quantum dots: fabrication of white fluorescent film and optical sensor applications. *Journal of Hazardous Materials* 2021; 125091. doi: 10.1016/j.jhazmat.2021.125091
34. Lim H, Liu Y, Kim HY, Son DI. Facile synthesis and characterization of carbon quantum dots and photovoltaic applications. *Thin Solid Films* 2018; 660: 672-677. doi: 10.1016/j.tsf.2018.04.019

35. Kahmann S, Shulga A, Loi MA. Quantum Dot Light-Emitting Transistors—Powerful Research Tools and Their Future Applications. *Advanced Functional Materials* 2020; 30: 1904174. doi: 10.1002/adfm.201904174
36. Jana J, Pal T. An account of doping in carbon dots for varied applications. *Natural Resources & Engineering* 2017; 2: 5-12. doi: 10.1080/23802693.2017.1421506
37. Atabaev TS. Doped Carbon Dots for Sensing and Bioimaging Applications: A Minireview. *Nanomaterials* 2018; 8: 342. doi: 10.3390/nano8050342
38. Jia Y, Hu Y, Li Y, Zeng Q, Jiang X, Cheng Z. Boron doped carbon dots as a multifunctional fluorescent probe for sorbate and vitamin B12. *Microchimica Acta* 2019; 186: 84. doi: 10.1007/s00604-018-3196-5
39. Shan X, Chai L, Ma J, Qian Z, Chen J, Feng H. B-doped carbon quantum dots as a sensitive fluorescence probe for hydrogen peroxide and glucose detection. *Analyst* 2014; 139: 2322-2325. doi: 10.1039/C3AN02222F
40. Wei Y, Chen L, Wang J, Liu X, Yang Y, Yu S et al. Rapid synthesis of B-N co-doped yellow emissive carbon quantum dots for cellular imaging. *Optical Materials* 2020; 100: 109647. doi: 10.1016/j.optmat.2019.109647
41. Ma Y, Chen AY, Huang YY, He X, Xie XF et al. Off-on fluorescent switching of boron-doped carbon quantum dots for ultrasensitive sensing of catechol and glutathione. *Carbon* 2020; 162, 234-244. doi: 10.1016/j.carbon.2020.02.048
42. Bourlinos AB, Trivizas G, Karakassides MA, Baikousi M, Kouloumpis A et al. Green and simple route toward boron doped carbon dots with significantly enhanced non-linear optical properties. *Carbon* 2015; 83: 173-179. doi: 10.1016/j.carbon.2014.11.032
43. Kırbıyık Kurukavak, Ç, Yılmaz T, Cetin S, Alqadasi MM, Al-Khawlyani, KM, Kus M. Synthesis of boron-doped CQDs and its use as an additive in P3HT:PCBM layer for efficiency improvement of organic solar cell. *Microelectronic Engineering* 2021; 235: 111465. doi: 10.1016/j.mee.2020.111465
44. Pan D, Zhang J, Li Z, Wu C, Yan X, Wu M. Observation of pH-, solvent-, spin-, and excitation-dependent blue photoluminescence from carbon nanoparticles. *Chemical Communications* 2010; 46: 3681-3683. doi: 10.1039/C000114G
45. Feng Q, Xie Z, Zheng M. Colour-tunable ultralong-lifetime room temperature phosphorescence with external heavy-atom effect in boron-doped carbon dots. *Chemical Engineering Journal* 2020; 420(2): 127647. doi: 10.1016/j.cej.2020.127647
46. Nazri NAA, Azeman NH, Luo Y, A Bakar AA. Carbon quantum dots for optical sensor applications: A review. *Optics & Laser Technology* 2021; 139: 106928. doi: 10.1016/j.optlastec.2021.106928
47. Valeur B, Berberan-Santos MN, Appendix: Characteristics of Fluorescent Organic Compounds, in (eds Valeur B. and Berberan-Santos MN) *Molecular Fluorescence*. Weinheim: Germany Wiley-VCH, 2012, pp. 521-550.
48. Horiba Scientific, *A Guide to Recording Fluorescence Quantum Yields*. Middlesex, UK: 2021.
49. Chirvase D, Parisi J, Hummelen JC, Dyakonov V. Influence of nanomorphology on the photovoltaic action of polymer–fullerene composites. *Nanotechnology* 2004; 15: 1317-1323. doi: 10.1088/0957-4484/15/9/035
50. Savenije TJ, Kroeze JE, Yang X, Loos J. The formation of crystalline P3HT fibrils upon annealing of a PCBM:P3HT bulk heterojunction. *Thin Solid Films* 2006; 511-512: 2-6. doi: 10.1016/j.tsf.2005.12.123
51. Anefnaf I, Aazou S, Schmerber G, Refki S, Zimmermann, Heiser T et al. Polyethylenimine-Ethoxylated Interfacial Layer for Efficient Electron Collection in SnO<sub>2</sub>-Based Inverted Organic Solar Cells. *Crystals* 2020; 10: 731. doi: 10.3390/cryst10090731
52. Tauc J, Grigorovici R, Vancu A. Optical Properties and Electronic Structure of Amorphous Germanium. *Physica Status Solidi (B)* 1966; 15: 627-637. doi: 10.1002/pssb.19660150224
53. Ismail Y, Soga T, Jimbo T. Effect of Composition on Conjugation Structure and Energy Gap of P3HT:PCBM Organic Solar Cell. *International Journal of New Horizons in Physics* 2015; 2: 87-93. doi: 10.12785/ijnhp/020208
54. Balogun S, Kolawole S, Kolawole Y. Effect of Thickness and Composition Ratio of Poly(3-Hexylthiophene) and [6,6]-Phenyl C60-Butyric Acid Methyl Ester Thin Film on Optical Absorption for Organic Solar Cell Fabrication. *Journal of Photonic Materials and Technology* 2019; 5 (1): 5-10. doi: 10.11648/j.jmpt.20190501.12
55. Müllerová J, Kaiser M, Nádaždy V, Šifalovič P, Majková E. Optical absorption study of P3HT:PCBM blend photo-oxidation for bulk heterojunction solar cells. *Solar Energy* 2016; 134: 294-301. doi: 10.1016/j.solener.2016.05.009
56. Li Z, Jiang K, Yang G, Lai JYL, Ma T et al. Donor polymer design enables efficient non-fullerene organic solar cells. *Nature Communications* 2016; 7: 13094. doi: 10.1038/ncomms13094
57. Langford JJ, Wilson AJC. Scherrer after sixty years: A survey and some new results in the determination of crystallite size. *Journal of Applied Crystallography* 1978; 11: 102-113. doi: 10.1107/S0021889878012844
58. Paulo S, Palomares E, Martinez-Ferrero E. Graphene and Carbon Quantum Dot-Based Materials in Photovoltaic Devices: From Synthesis to Applications. *Nanomaterials* 2016; 6: 157. doi: 10.3390/nano6090157

59. Horcas I, Fernandez R, Gomez-Rodriguez JM, Colchero J, Gomez-Herrero J et al. WSXM: A Software for Scanning Probe Microscopy and a Tool for Nanotechnology. *The Review of Scientific Instruments* 2007; 78: 013705. doi: 10.1063/1.2432410
60. Tan JK, Png RQ, Zhao C, Ho PKH. Ohmic transition at contacts key to maximizing fill factor and performance of organic solar cells. *Nature Communications* 2018; 9: 3269. doi: 10.1038/s41467-018-05200-w
61. Carey GH, Abdelhady A, Ning Z, Thon SM, Bakr OM et al. Colloidal Quantum Dot Solar Cells. *Chemical Reviews* 2015; 115: 12732-12763. doi: 10.1021/acs.chemrev.5b00063
62. Mihailetchi VD, Blom PWM, Hummelen JC, Rispens MT. Cathode dependence of the open-circuit voltage of polymer:fullerene bulk heterojunction solar cells. *Journal of Applied Physics* 2003; 94: 6849-6854. doi: 10.1063/1.1620683
63. Vandewal K, Oosterbaan WD, Bertho S, Vrindts V, Gadisa A. Varying polymer crystallinity in nanofiber poly(3-alkylthiophene):PCBM solar cells: Influence on charge-transfer state energy and open-circuit voltage. *Applied Physics Letters* 2009; 95: 123303. doi: 10.1063/1.3232242
64. Jeong S, Kon MS, Kim JH, Kim KH, Cho YS et al. Synthesis of a thiophene derivative and its effects as an additive on the performance of solar cells. *Molecular Crystals and Liquid Crystals* 2019; 678: 121-130. doi: 10.1080/15421406.2019.1597538